# Chapter-5

# Overlapping large polaron tunnelling in lanthanum silicate oxyapatite

**Publication:** ***Ashishkumar Yadav, Priyanka A. Jha, Pardeep K. Jha, Neetu Jha and Prabhakar Singh,*** *2022 J. Phys.: Condens. Matter in press DOI: https://doi.org/10.1088/1361-648X/acad53*

# CHAPTER 5: Overlapping large polaron tunnelling in lanthanum silicate oxyapatite

## 5.1 INTRODUCTION

Solid oxide ion conductors play a significant role in electricity conversion devices (solid oxide fuel cells (SOFCs)) as an alternative energy. SOFC is an electrochemical device which requires high temperature (> 1000 K) for its operation [110]. The recent surge in the energy demand comes from the domestic sector where high temperature devices are generally restricted, this makes SOFC out of contest as a popular choice of portable alternative energy sources. Low temperature (working between 500- 800 K) fast oxide ion conductors (FOICs) can solve this problem [110], [147] . The ionic conductivity of the high temperature FOICs generally decreases sharply with decrease in the temperature[147] hence such FOICs cannot be used in low temperature SOFC (IT and LT-SOFC). Thus, there is quest for FOICs at low temperatures.

The apatite based FOICs(discovered by Nakayama in 1995)[148] like perovskite based FOICs [149]–[151] showed high ionic conductivity in low temperature regime (LTR) [147], [152]–[159] . Among these FOICs, due to its anisotropic ion con-duction ($\frac{\sigma_c^{\parallel}}{\sigma_c^{\perp}} > 10$), lanthanum silicate oxyapatite i.e., $La_{10-\alpha}^{3+}(SiO_4)_6^{4-}O_{2+\delta}^{2-}$ $(LSO)$ is one of the most interesting materials[160], [161] [15, 16]. In polycrystalline samples, grain alignment and doping are the two common methods to get the desired properties in the sample, the same has been

employed by various research groups in the last few years [152]–[155], [157]–[159], [161]–[165] . Various doping such as Al, Mg at B-site and Alkaline earth and rare earth substitutions at A-site have been done in order to get conductivities in the range of 1 S/cm but unfortunately, conductivity is achieved in the range of 10-50 mS/cm[129] [147], [152]–[159]. To explain this the two kind of conduction mechanism, namely, push-pull and interstitial[166] are well described for the oxyapatite. In the push-pull conduction mechanism, interstitial oxygen cooperatively migrates with O4 to the most stable interstitial O site with the lowest potential barrier of 0.01 eV with site energies in the range of 0-0.25 eV. Thus, it is supposed to occur in the ideal perfect crystal lattice with no defects and no La vacancies and migration is comparable to short range hopping in the stable zone. In the other mechanism where $O_2$ oxygen is involved, the potential barrier is 0.53eV with the site energy 0.82eV[167].The long range conduction mechanism consists of long pathways in the O4 column with the cooperative interstitial mechanism. It leads to strong anisotropy in the oxygen ion conduction being reported by Nakayama in 2013[168]. Various experiments and theoretical studies predict that $O_{int}$ (interstitial Oxygen) promotes cooperative movements between the O4 ion and excess oxygen is introduced as interstitial charge carriers to maintain electrical neutrality with La ions. There are 4 channels proposed for the conduction. Channels no. 1 and 2 are formed by the oxygen vacancies in between La(4f)-O4, channel no. 3 is nearest to the Si vacancy site and channel no. 4 is linked to the formation of oxygen Frenkel defects . Despite of these studies, the dynamics which can explain the ion

conduction alteration with structural disorder (polaronic hopping) is still scarce at large in spite of the fact that there is correlation between ion diffusion and polaron prevalence in ionic conductors[169]–[171]. In ionic conductors' conduction is a prototype of polarons and the conduction is possible due to the jump of mobile ions with a large phonon amplitude. The polarons are classified in two categories on the basis of interaction as strong coupling and weak coupling. The strong coupling of polarons also come under the self-trapping phenomenon and further categorized as large and small polarons. The large polarons have the coherence length greater than lattice parameter while small porons have coherence length lesser than lattice parameter. Further, the lowering of activation energy assists the enhanced phonon amplitudes which assist the jump of mobile ions and ion conduction [172]. Thus, there is scope of conductivity enhancement in polycrystalline LSO by understanding the role of phononic contributions. In order to check the correlation between polaron hopping and ion diffusion, we are here investigating the alteration in the structural disorder and dynamics with Ca-substitution in LSO. To investigate this correlation, we have analyzed the structural, low frequency ($10\ s^{-1} < \omega \leq 10^6\ s^{-1}$) conductivity, optical absorption, valence band edge through photoemission spectroscopy and dependent conductivity.

## 5.2 Materials and Methods

### 5.2.1 Sample preparation

Apatite based material lanthanum silicates (LSO) and Calcium (Ca) doped LSO were prepared using solid state route method. The starting materials

were $La_2O_3$ (Sigma-Aldrich 99.9%), $SiO_2$ (Sigma-Aldrich 99.5 %) and $CaCO_3$ (99%) and weighed in stoichiometric proportions. The samples were thoroughly ground using mortar and pestle for 30-40 min. The obtained product was mixed with propanol and ball milled using zirconia ball for 6 h. After ball milling the dried powder was calcined at 1000 °C for 8 h and phase determination of the calcined powder was done. Further, calcined powder was then ground and mixed with Polyvinyl alcohol (PVA) as a binder and pressed at 7 MPa to turn for palletization and pellets were then sintered at 1375 °C for 14 h at the heating rate of $5^o$ $min^{-1}$.

## 5.3 Characterization techniques

The phase identification of calcined powder and sintered pellets was done through Rigaku Mini ex powder diffractometer with Cu- Kα radiation (λ = 1.540598 Å) and Ni filter in the range $2\theta \approx 20° - 80°$ with a step size of 0.02º. The XRD data was refined with $P6_3/m$ symmetry using FullProf Suite software package in structural Rietveld mode. After applying zero correction of the instrument, Pseudo - Voigt peak profile was used for refinement. The structure is studied using Diamond 3.0 software and bond distances along with lattice parameters are obtained. Further, bond valence sum calculation is done using Full Prof software to find the percolation energy. The thermogravimetric analysis of the calcined powders was carried out simultaneous TG-DSC (Mettler Toledo, Germany) thermal analyzer in the temperature range 30-1000 ºC at a constant heating rate of 10 ºC $min^{-1}$ in the nitrogen atmospheres. The density of prepared sintered pellets was measured using density kit (Sartorius,

BSA2245CW). The elemental compositions (EDAX) of the sintered pellets were characterized using scanning electron microscopy (EVO - Scanning Electron Microscope MA15 / 18). The average grain size was calculated using the linear intercept method. The electrical measurements were done using LCR meter (Wayne Kerr 6500P) in the temperature range 100 ºC to 700 ºC over the frequency range of between 20 Hz and 1 MHz. The elemental composition was further verified using X-ray photoelectron spectroscopy (Kratos Amicus model) high performance analytical instrument utilizing Mg target under 10− 6 Pa pressure. The UV-VIS absorption study was carried out using JASCO V-770 ultraviolet visible (UV) spectrometer. The Current-Voltage (I V) curve measurement is performed using Keithley 2450 source meter.

## 5.4 RESULTS AND ANALYSIS

The structural and dynamic disorder are important feature for ion conduction. In order to understand the modification caused by Ca-substitution at La-site in $La_{10-\alpha}^{3+}(SiO_4)_6^{4-}O_{2+\delta}^{2-}$ $(LSO)$ ; with α = 0.33 system and its influence on the ion transport behavior, we performed structural and electrical characterization in details.

### 5.4.1 Structural Studies

The Rietveld refinement of X-ray diffractograms done with $P6_3/m$ symmetry using Full Prof Suite package with Pseudo-Voigt peak profile is shown in Fig. 5.1(a)). The goodness of fit ($\chi^2$) is lying within the appreciable range (Fig.5.1(a)). We have observed single phase lanthanum silicate and at x = 0.05, a secondary phase at $2\theta \approx 28^o$ corresponding to $SiO_2$ is observed (JCPDS file No. 89-1813). But this secondary phase diminishes at x = 0.1 and one more phase at $2\theta \approx 26^o$ appears at x = 0.15 sample corresponding to $SiO_2$ is observed (JCPDS file No. 89-1813). In addition, the splitting of the peak corresponding to $2\theta \approx 32^o$ disappears with the increase in x (Fig.5.1(b)). However, the peak is observed to be shifted towards a higher angle at x = 0.15 whereas there is nominal shifting at lower x content.

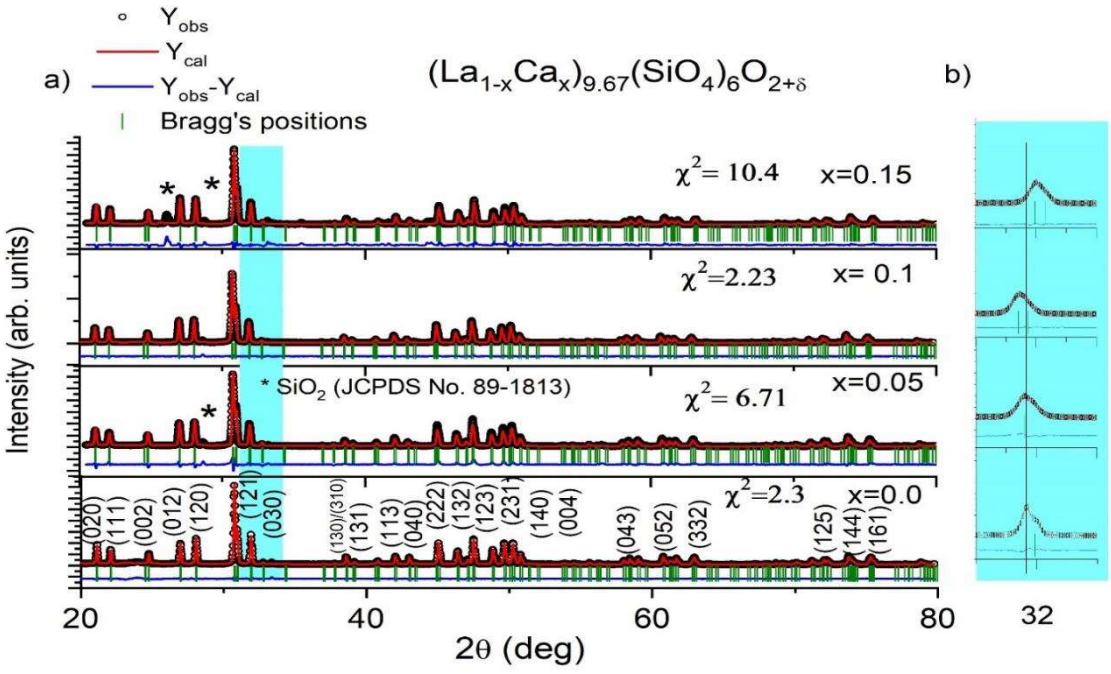


**Figure. 5.1** (a) Rietveld refinement of X-ray diffractograms with $P6_3/m$ symmetry using Full Prof Suite package with Pseudo-Voigt peak profile. The goodness of fit ($\chi 2$) is lying within the appreciable range (Fig.5.1(a)). (b) splitting of the peak corresponding to $2\theta \approx 32^o$ disappearing with the increase in x.

The lattice parameter 'c' and volume of ion mobility has shown a similar trend with x (Fig.5.2 (a-b)). Further, the lattice parameters 'a' and 'b' have shown similar behaviour with x like La1(6h)-O4 bond length. Thus, for Ca substitution, the solid solubility limit exists up to x = 0.1. However, x = 0.15 showed exceptional behavior due to secondary phase formation of $SiO_2$. The bond length maximum at x = 0.1 suggests the formation of big La-6h triangles that surround the O4 channel. Further, this is suggesting the formation of more La vacancies at x = 0.1 instead of other substituted samples. The occupancy obtained from Rietveld refinement is also showing La deficient samples.

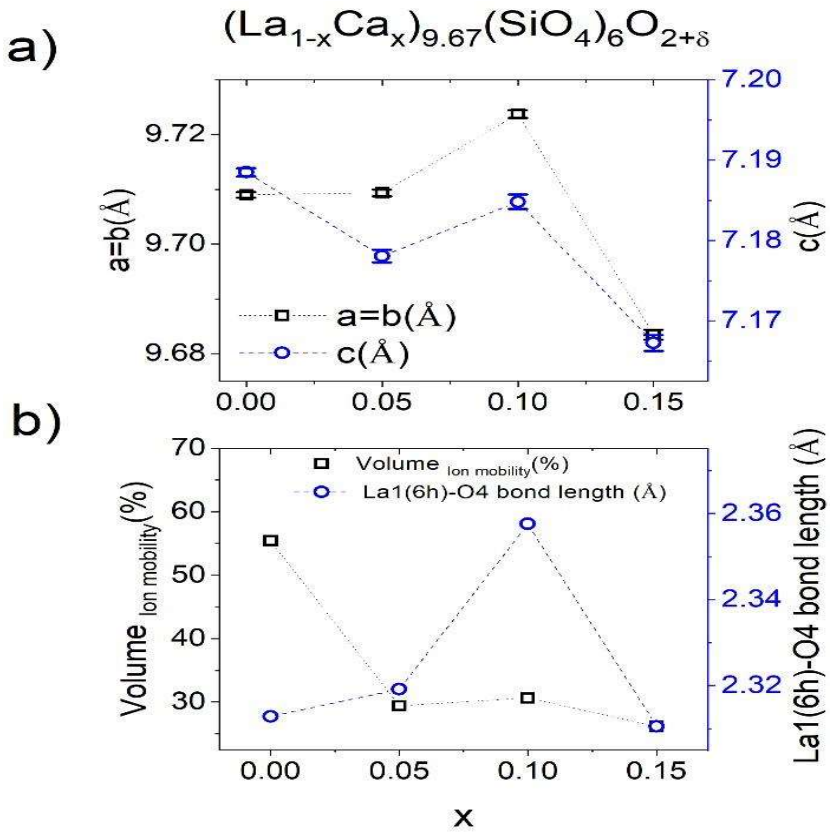


**Figure 5.2** (a-b) Variation of Lattice parameters, La1(6h)-O4 bond distance of Ca modified $(La_{1-x}Ca_x)_{9.67}(SiO_4)_6O_{2+\delta}$ (x = 0.0, 0.05, 0.10 and 0.15)

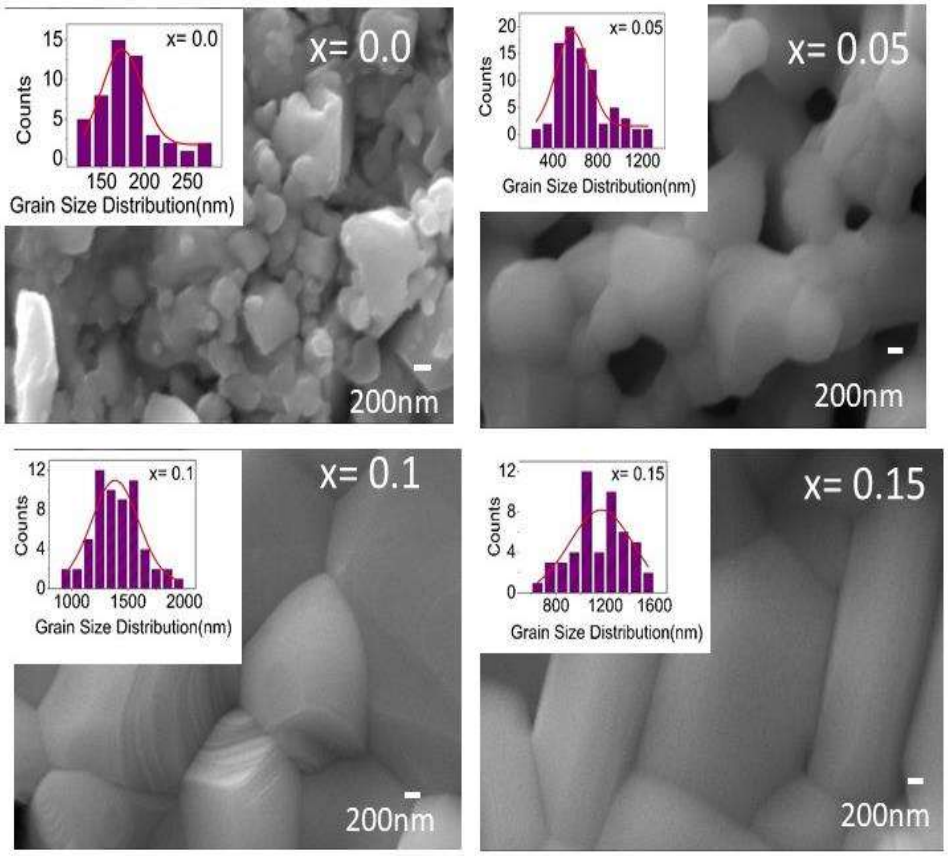


**Figure 5.3**. SEM micrographs and grain histograms of Ca modified $(La_{1-x}Ca_x)_{9.67}(SiO_4)_6O_{2+\delta}$ (x = 0.0, 0.05, 0.10 and 0.15)

The polycrystalline microstructure is observed for x = 0.0 and with the increase in x ($(La_{1-x}Ca_x)_{9.67}(SiO_4)_6O_{2+\delta}$ (x = 0.0, 0.05, 0.10 and 0.15)), the porosity reduces with the increase in grain size up to x = 0.1 (Fig. 5.3). Further, hexagonal grains are observed up to x = 0.1. Exceptionally, for x = 0.15, grains are stretched and appear like stretched hexagons (rods). The average grain size has been estimated using grain size histograms and linear intercept method. The secondary phases visible in XRD cannot be seen in SEM micrographs of x= 0.15 sample. To further analyze the secondary

phase, elemental mapping suggests the inhomogeneous distribution of Si at grain and grain boundaries. Further, to determine the elemental concentration we have used XPS and TGA.

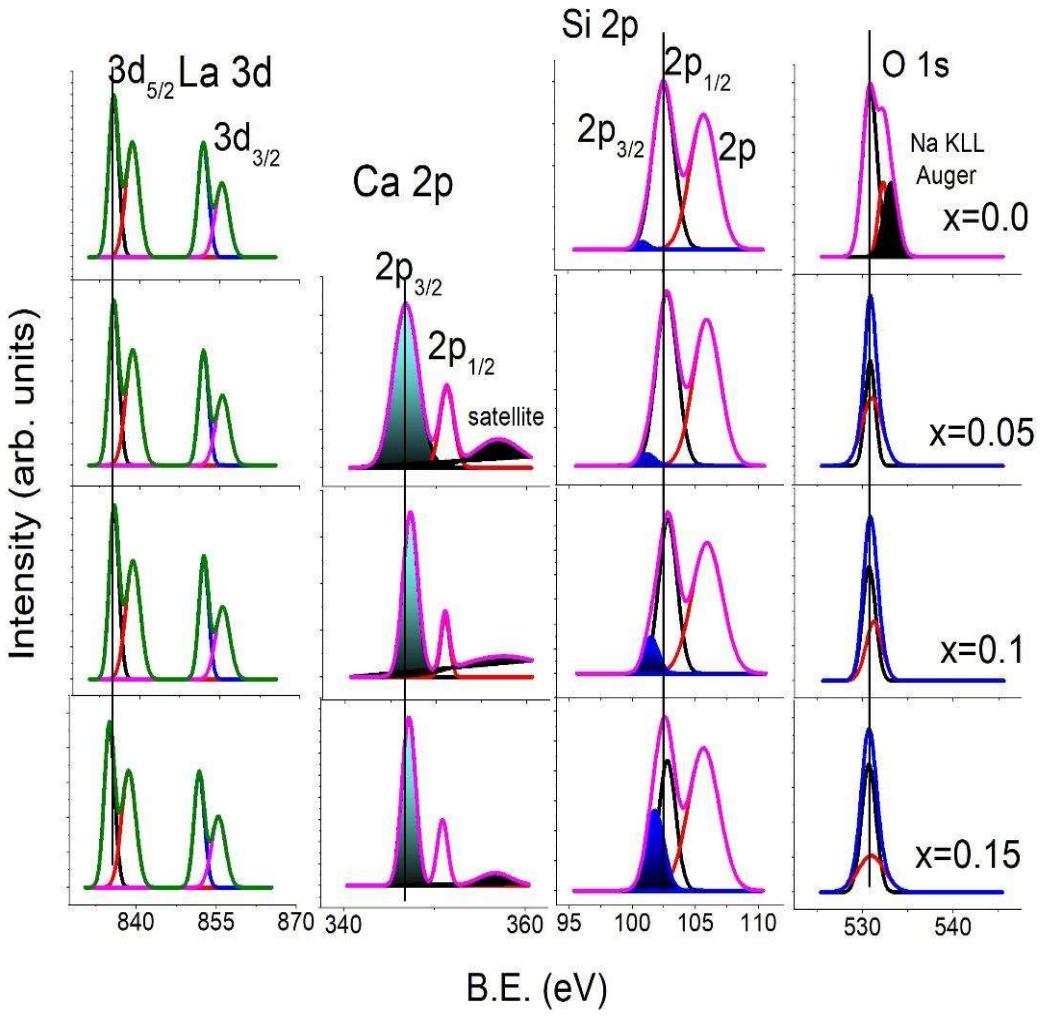


**Figure 5.4** Deconvoluted X-ray photoelectron spectroscopy measurements of Ca modified $(La_{1-x}Ca_x)_{9.67}(SiO_4)_6O_{2+\delta}$ (x = 0.0, 0.05, 0.10 and 0.15)

X-ray photoelectron spectroscopy measurements of the $La_{1-x}Ca_x)_{9.67}(SiO_4)_6O_{2+\delta}$ (x = 0.0, 0.05, 0.10 and 0.15) (Fig. 5.4) are analyzed by analyzing the standard look up table and deconvolution of the elemental data. The La 3d spectrum shows three chemical

states corresponding to $La_2O_3$, $La(OH)_3$ and $La_2CO_3$ with well-defined and separated spin components and energies (ΔE) corresponding to 4.6 eV, 3.9 eV and 3.5eV, respectively. In the present case, we have observed ΔE ~ 4.0eV corresponding to the spin orbit splitting corresponding to La $(OH)_3$. Further, no peak shifting is observed for $La3d_{5/2}$ components. Here, we can also see the individual spin orbit component splitting. In Ca2p spectra (< 1eV), chemical shift with the increase in x is observed. Further, Ca2p has spin orbit components with ΔE ~ 3.5eV. Here, shake-up satellite is also observed but it cannot be resolved into its components as standard ones. Si 2p spectrum exhibits ΔE ~ 0.63 eV i.e. very close spin orbit splitting. Thus, we have observed asymmetric peaks corresponding to Si 2p. Further, the intensity of Si 2p3/2 content is observed to increase with the increase in x showing the formation of secondary phase. However, chemical shift of the spin orbit component is also observed. In O spectra, O 1s peak at ~ 529 eV is linked to the metal and O bond (La-O, Si-O and Ca-O) while, $2^{nd}$ peak of O belongs to metal-OH bond. Oxygen vacancy concentration is linked to the ratio of peak area corresponding to the M-O and M-OH bond. Here, the ratio of area of peaks is observed to decrease with the increase in x and showing the decrease in oxygen vacancy concentration with x. Thus, oxygen content is observed to increase and vacancy is observed to decrease with the increase in x. Further, Na KLL Auger peak is observed in x = 0.0 and with the increase in x, Auger peak diminishes. Simultaneously, intensity of satellite peak in Ca 2p spectra is increasing with x due to metal ligand interaction i.e. interaction of s- orbital of Ca and p-orbital of O (s-p interaction). In addition, the formation of $La(OH)_3$ suggests the formation of La vacancies and the samples are found to be La and Si deficient from the occupancies observed from the Rietveld refinement.

Thus, the formation of oxygen/ lanthanum and silicon vacancies has been analyzed through Thermogravimetric analysis in $N_2$ atmosphere.

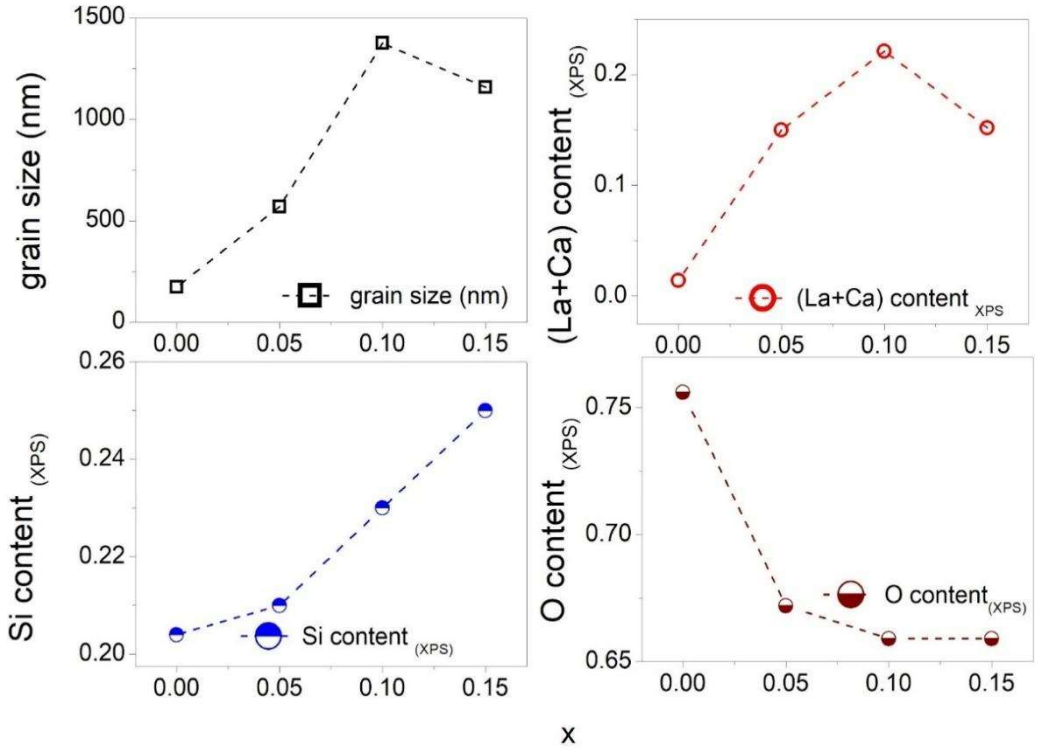


**Figure 5.5** (a) Grain size obtained from SEM micrographs (grain histograms) (b) La content extracted from XPS (c) Si content from XPS (d) O content from XPS (lines are a glide to eye)

It is observed in Fig. 5.5 that grain size (obtained from grain size histograms) is increasing with x with an exception at x = 0.15. The trend of grain size is like the trend in (La+ Ca) content and further, grain morphology changes from porous to dense with the increase in x up to x = 0.1 and changes from faceted to rough at x = 0.15. This change indicated grain- boundary roughening. With the increase in La content at x = 0.1, rough grain boundaries have lower driving force for grain-boundary movement, thus, leading to the

increase in grain size. With the further increase in x and eruption of the secondary phase, the driving force elongated grains to perpendicular (XY) direction instead of XX direction. Further, Si and O are behaving opposite to each other i.e., with the increase in x Si content increases and O content decreases.

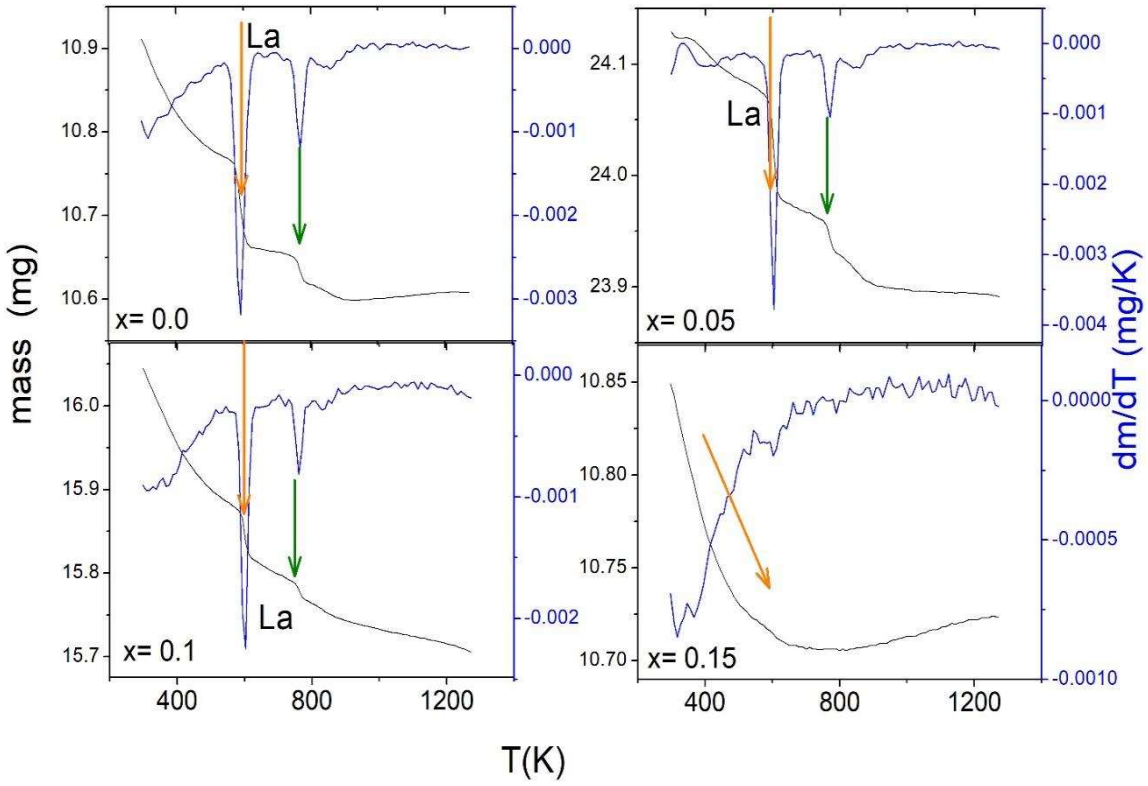


**Figure 5.6** Thermogravimetric curves for Ca modified $(La_{1-x}Ca_x)_{9.67}(SiO_4)_6O_{2+\delta}$ (x = 0.0, 0.05, 0.10 and 0.15) showing the variation of mass loss and dm/dT with temperature

A gradual mass loss is observed in Thermogravimetric curves for Ca modified $(La_{1-x}Ca_x)_{9.67}(SiO_4)_6O_{2+\delta}$ (x = 0.0, 0.05, 0.10 and 0.15). Further, up to x = 0.10, two kinks are observed at ~500 K and 800 K (shown by orange and green arrows in Fig. 5.6). These kinks correspond to the weight loss due to La as the weight loss observed in both

the kinks is ~ 5.8%. The La deficiency observed is in accordance with the La content estimated from XPS and Rietveld refinement. Further, EDX data is also supporting the estimations done from refinement, XPS and TGA.

$$5La_2O_3 + 6SiO_2 \rightarrow La_{10-\alpha}Si_6O_{26+\delta} + \alpha V_{La}^{3+} + \delta V_O^{2-}$$

| Table5.1 δ obtained from TGA and XPS | | |
|---|---|---|
| Composition | α obtained from TGA_$N_2$ atm | La obtained from XPS |
| x = 0.0 | 0.019 | 0.014 |
| x = 0.05 | 0.013 | 0.149 |
| x = 0.1 | 0.008 | 0.221 |
| x = 0.15 | 0.014 | 0.152 |

Here, the ratio of area of peaks corresponding to metal-O and metal-OH is observed to decrease with the increase in x and showing the decrease in oxygen vacancy concentration with x. Thus, oxygen content is observed to increase and vacancy is observed to decrease with the increase in x. Further, Na KLL Auger peak is observed in x = 0.0 and with the increase in x, Auger peak diminishes. Simultaneously, intensity of satellite peak in Ca 2p spectra is increasing with x due to metal ligand interaction i.e. Interaction of s- orbital of Ca and p-orbital of O (s-p interaction). In addition, the formation of $La(OH)_3$ suggests the formation of La vacancies and the samples are found to be La and Si deficient from the occupancies observed from the Rietveld refinement. Thus, the formation of oxygen/

lanthanum and silicon vacancies has been analyzed through Thermogravimetric analysis in N2 atmosphere. A gradual mass loss with two kinks (at ~500 K and 800 K) are observed in thermogravimetric curves and these kinks correspond to the weight loss due to La. The La deficiency observed is in accordance with the La content estimated from XPS and Rietveld refinement (details are in supplementary). From impedance spectroscopy, we observed diffusive spectra at low frequency in all samples while at high frequency end the behaviour almost resistive with very low impedance which is signature of ion-diffusion[173]. The apatite structure does not go under structural phase transition till high temperature as high as 1473 K, there- fore electrical behavior till 1000 K can be easily found in correlation with structure at room temperature. The conductivity- frequency -temperature (σ-ω-T ) plots are drawn for each sample. These frequency ($10\ s^{-1} < \omega \leq 10^6\ s^{-1}$) dependent conductivity isotherms (548 -973 K) (see supplementary) are fitted with Jonsher Power law (JPL)[174][30],

$$\sigma = \sigma_{dc}\left(1 + \left(\frac{\omega}{\omega_h}\right)^p\right) \qquad ---------(5.1)$$

Through the fitting of conductivity isotherms with JPL, dc conductivity ($\sigma_{dc}$), hopping frequency ($\omega_h$) and exponent($p$) are extracted.

## 5.5 Temperature dependence conduction behaviour

### 5.5.1 dc Conductivity

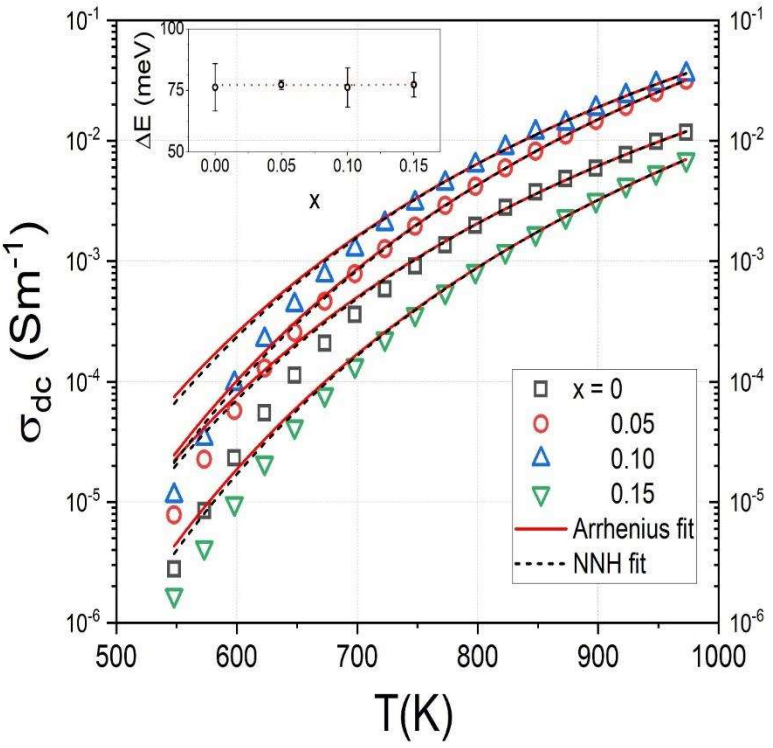


**Figure 5.7.** Arrhenius and NNH fitting of $\sigma_{dc}$-T curves for x = 0, 0.05, 0.1 and 0.15 in $(La_{1-x}^{3+}Ca_{x}^{2+})_{9.67}(SiO_4)_6^{4-}O_{2+\delta}^{2-}$ system. (Inset) shows the difference in the two activation energies is ΔE ~ 75 meV

Fig 5.7 $\sigma_{dc} - T$ plot for all samples it is clearly visible that with x conductivity increase upto x = 0.1 there after it decreases for x = 0.15. The conductivity in these apatites strongly depends on the activation energy. Therefore, $\sigma_{dc} - T$ curves are fitted with Arrhenius relation ($\sigma = \sigma_0 \exp\left(-\frac{E_a}{k_\beta T}\right)$,solid red line) and also with nearest neighbour hopping (NNH) model ($\sigma T = \sigma_0 \exp(-\frac{E_a}{k_\beta T})$, dashed black line). For T>700K both fitting matches well, however NNH fitting has better correlation ( $R^2$>0.999) with experimental data

which confirm nearest neighbour hopping in these samples. Here, with substitution of Ca, no particular trend could be observed for activation energy as observed in the structural and microstructural parameters. The activation energies (NNH) are $E_h$~ 0.76,0.85,0.74 and 0.88 eV respectively. However, the interesting feature is the difference in the two activation energies is $\Delta E \sim 75$ meV (fig 1(inset)). It is necessary to mention that 75 meV is a significant value which indicates oxygen vacancy assisted polaron conduction[175], [176] . However, in the present context, it is the difference which is 75meV and beyond our present understanding. The high activation energy (0.85 eV) for x = 0.05 is due to porosity [177], [178]as observed in microstructures, while for x = 0.15, it is due to $SiO_x$ phase, which provide more scattering thus more resistance is offered. Thus hereafter, we are comparing the hopping conduction mechanism in the samples with same activation energy i.e., x = 1.0 ($E_h$~0.74 eV) with undoped LSO i.e., x = 0 ($E_h$~0.76 eV).

## 5.5.2 The universal exponent 'p'

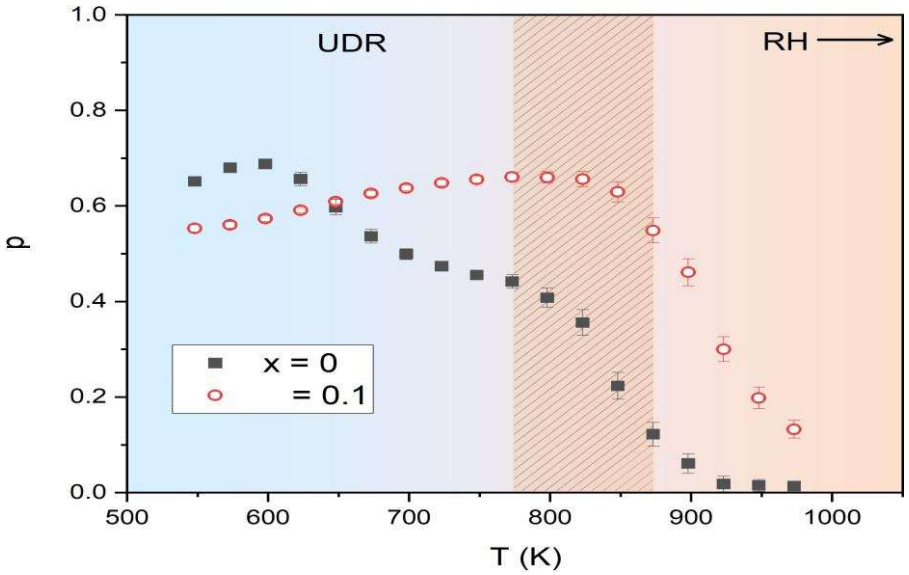


**Figure 5.8.** The universal exponent (p)-Temperature(T) plot for x=0, x=0.1 in $(La_{1-x}^{3+}Ca_x^{2+})_{9.67}(SiO_4)_6^{4-}O_{2+\delta}^{2-}$ system

The universal exponent ($p$) behavior can suggest how frequency dependence of conduction behaviour is altering with thermal activation. Therefore p-T curves are drawn for the two samples i.e. x=0.0 and x=0.1 (Fig 5.8). It is observed for both the samples that the exponent is continuously decreasing for temperature range (773-873 K). Beyond 873 K, $p \rightarrow 0$ suggesting diffusion and hence transport is almost frequency and temperature independent for x=0.0. However, $p \rightarrow 0$ at a higher temperature >1000 K for x=0.1. Consequently, lead to ions hopping between two sites and does not have any information of the previous site, therefore random hopping is approached by both the samples once thermal energy exceeds ~ 75 meV. The major difference between two samples is appearing for temperature 548 K > T > 773 K. Here both the samples show the universal dielectric relaxation[174] [30]. For x=0, there is maximum at 598 K with p ~ 0.7 while for x=0.1, there is maximum at 823 K with p ~ 0.65. Thus, the exponent due to correlated barrier hopping (CBH) and OLPT[179] which will be verified later. Nevertheless, p < 1 suggests the behaviors for x = 0, suggests overlapping large polaron tunnelling (OLPT) while for x = 0.1 conduction is appearing sublinear behavior for both the samples.

## 5.6 Frequency dependent conductivity behaviour

### 5.6.1 The exponent parameter (s)

The shape of $\sigma_{dc}$ −T curves (Fig.5.7) hints for quantum mechanical tunneling (QMT), CBH and OLPT [179]. The limitation with the universal exponent p is that it itself is not frequency dependent while the tunnelling process is assisted by phonon interaction [179]. Thus, we require other formalism for exponent which must be frequency and temperature dependent, for this we extracted the exponent parameter(s),

$$s = \frac{d \ln \sigma(\omega)}{d \ln \omega} \qquad ----------[5.2]$$

The variation of s for the two samples are shown in the T- $\omega$ contour plot (Fig 5.9). For both samples, the parameter 's' is frequency as well as temperature dependent. For x=0, it is observed that with temperature s-value increases from ~0.86 to ~0.95, while for x=0.1, s-value increases from ~0.92 to ~0.97. Here it is important to mention that the temperature dependence of 's' is not similar to the behaviour of universal exponent 'p'. As far as frequency dependence is concerned, the s-value decreases with frequency for both the samples. This suggests thermal activation favours some trapped charge carriers to hop between sites with unequal barrier height, therefore possibility of CBH and QMT is ruled out. However, we fitted the s-T curve (at $\omega$ ($s^{-1}$) $\approx 10^2$, $10^3$, $10^4$, $10^6$) with CBH , QMT and OLPT and found that curves are well fitted with OLPT [180] (eqn 5.3) (Fig 5.10).

$$s = 1 - \left(\frac{1}{R'}\right)\frac{\left[4 + \frac{6}{R_E}\right]}{\left(1 + \frac{1}{R_E}\right)^2} \qquad -------[5.3]$$

Here, $r_0', R'$ and $R_E$ are reduced quantities which are defined as per eqn. 5.4

Here $\frac{1}{R_E} \equiv \beta E_{h0} r_0'/R'^2$ , $r_0' = 2\alpha r_0, R' = 2\alpha R$ $\qquad ----[5.4]$

Further, $\beta \equiv 1/K_B T$, $E_{h0} = E_h/(1 - \frac{r_0}{R})$ , here $r_0$ is polaron radius, R is tunneling distance and $E_h$ is hopping energy. Here a function $\mathcal{F}(\omega, T)$ is defined as per eqn. 5.5 for tunnelling distance (R) expressed by eqn. 5.6.

$$\mathcal{F}(\omega,T) \equiv \ln\left(\frac{\omega_h}{\omega}\right) - \beta E_{h0}; where\ \beta \equiv \frac{1}{k_B T} \qquad ------[5.5]$$

$$R(\omega) \equiv R = \frac{1}{4\alpha}\mathcal{F}(\omega,T) + \{\mathcal{F}^2(\omega,T) + 8\alpha r_0 \beta E_{h0}\}^{\frac{1}{2}} \qquad -----[5.6]$$

We observed that after fitting the exponent 's' with the OLPT model and using equations 5.4-5.6, the tunnelling distance (R), polaron radius($r_0$) are extracted. Fig. 5.11(a) shows the variation of $E_{h0}$ with R for x=0.0 and x=0.1. It is observed that the tunnelling distance reduces with the increase in frequency. The smallest tunnelling distance is observed at $\omega = 10^6\ s^{-1}$ (3.70 Å for x=0.0 and 2.39 Å for x=0.1), which is greater than La1-O3 bond lengths 'a' ($\lesssim 2.3$ Å). Further, the polaron radii at frequency $\omega = 10^6\ s^{-1}$ for x=0.0 sample is 19.28 Å and for x=0.1 sample, it is 4.31 Å i.e., $r_0 > a$. Moreover, it can also be seen (Fig. 5.11(b)) that at lowest frequency, R is maximum and $E_{h0}$ is minimum. Further, with the increase in frequency, $E_{h0}$ is increasing. It is evident that hopping energy decreases with tunnelling distance but the spatial extension of polarons is much larger for x=0.1. It indicates the overlap of potential wells of the neighbouring sites because of long similar range Coulomb interaction [179]. Further, extracted value of Frohlich coupling constant $\alpha$ is very high >3 and nearly similar for both samples, indicating strong electron-phonon coupling. This correlation between hopping energy and polaron radius with massive polaron formation suggests the ionic nature of the compounds.[181].

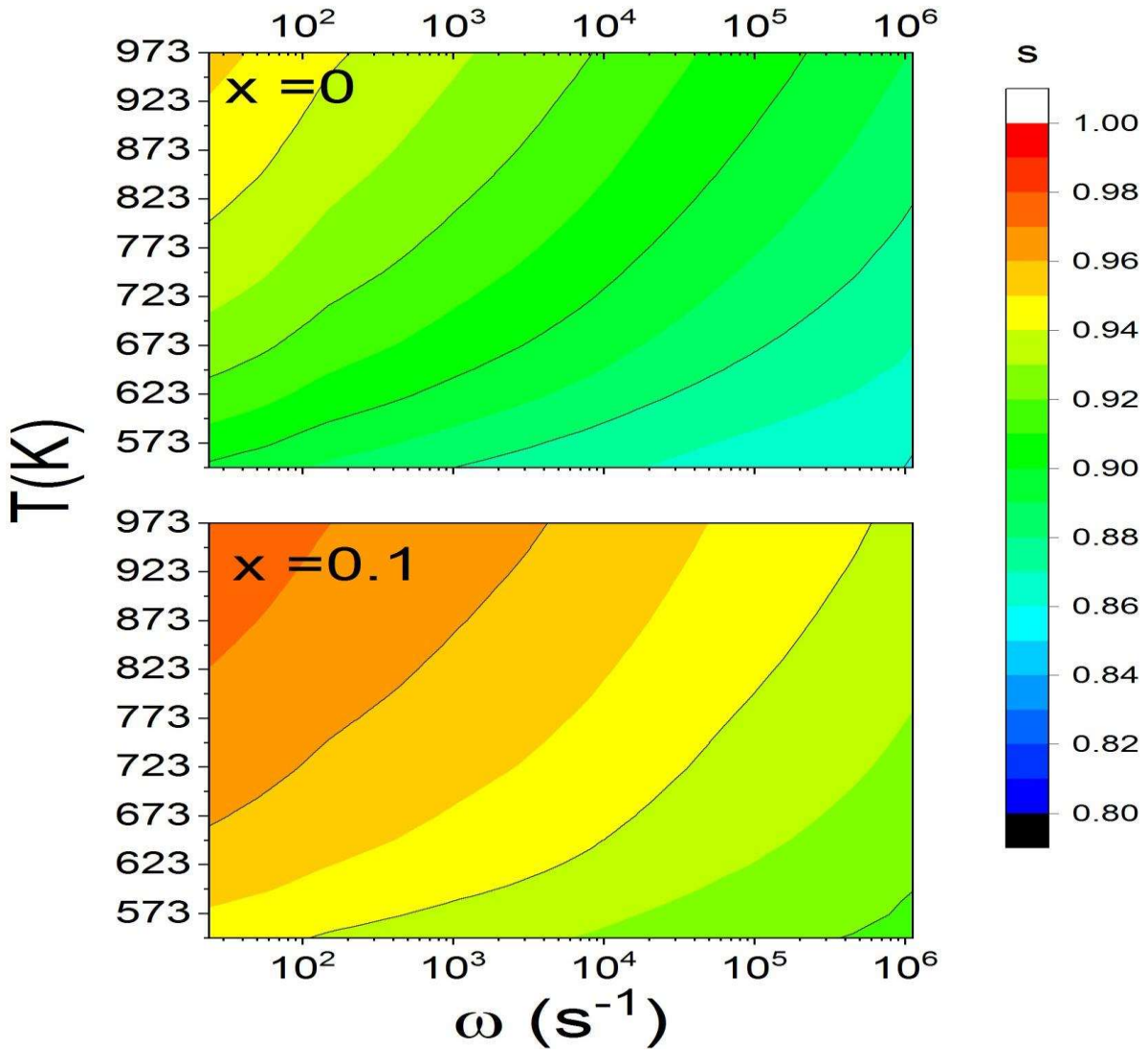


Figure 5.9. Two-dimensional contour plot of s versus T and $\omega$ for x = 0, x = 0.1 in $(La^{3+}_{1-x}Ca^{2+}_{x})_{9.67}(SiO_4)^{4-}_{6}O^{2-}_{2+\delta}$ system.

## 5.7 Optical absorption

Electronic portion To get energetics of large polaron formation in these two samples, we have performed the optical absorption study. The threshold for the photo

dissociation of large polarons is estimated at $3E_P$ , where at $E_P$ is ( electronic portion of) large polaron binding energy [182], [183].

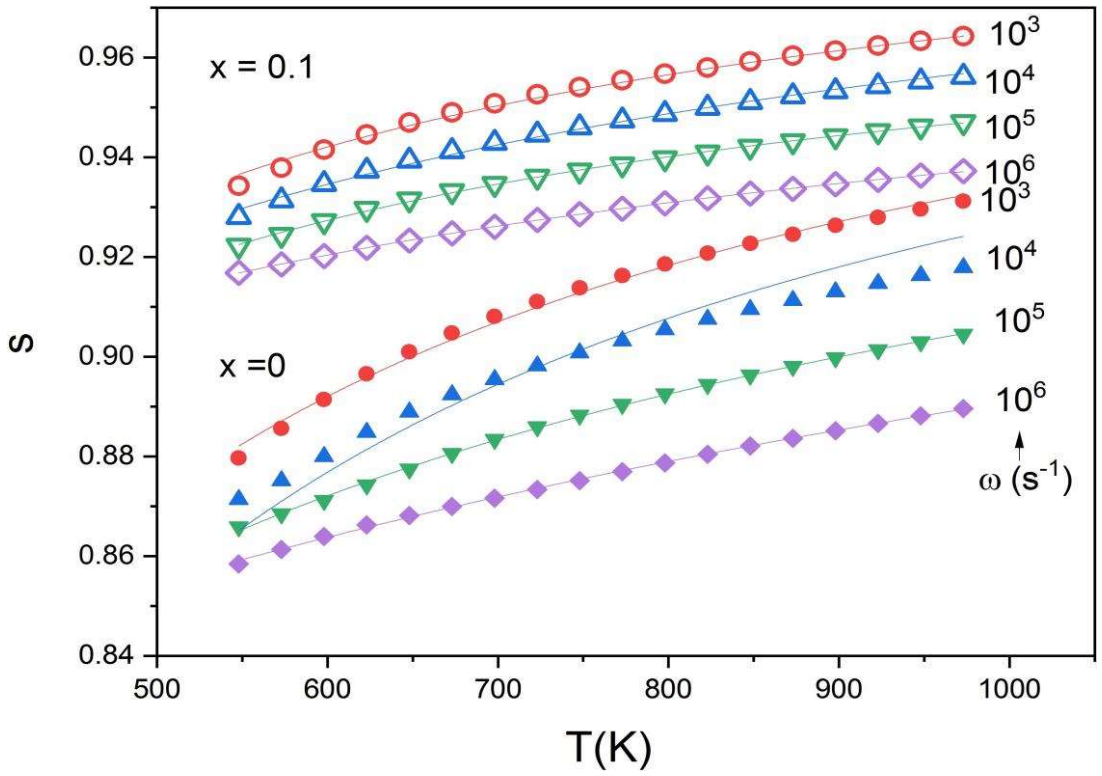


**Figure 5.10.** Overlapping Large Polaron Tunnelling (OLPT) fitting of parameter s-T curves at $\omega$= $10^3$, $10^4$, $10^5$ and $10^6$($s^{-1}$) for $(La^{3+}_{1-x}Ca^{2+}_{x})_{9.67}(SiO_4)^{4-}_{6}O^{2-}_{2+\delta}$ system

The estimated value of $E_P$ ~1.13 eV for both the samples. The normalized small absorption peaks for photon energy $E < 3E_P$; while strong absorption for $E > 3E_P$. For $E < 3\ E_P$, carrier optical (large polarons) absorption spectrum for x = 0 and 0.1 is plotted (Fig. 5.12(a)) in terms of $E_p$. We can see some absorption indicates phonon-electron interaction and therefore absorption is due to photoexcitation of polarons to bound states in the deformable ion continuum. Before going into further details, it would be helpful to get some idea of

electronic band structure. For this we have inspected valence band (VB) spectra using XPS study (Fig. 5.12(b) (inset)) and observed VB edge at 2.13 eV from fermi level ($E_f$). We can see some photoemission at fermi level which is due to mobility transfer attributing to polarons[184]. Interestingly, photoemission is higher for x = 0.1 like optical absorption indicates higher mobility. Also, the direct band gap is estimated (from Tauc plots; Fig.5.12(b)

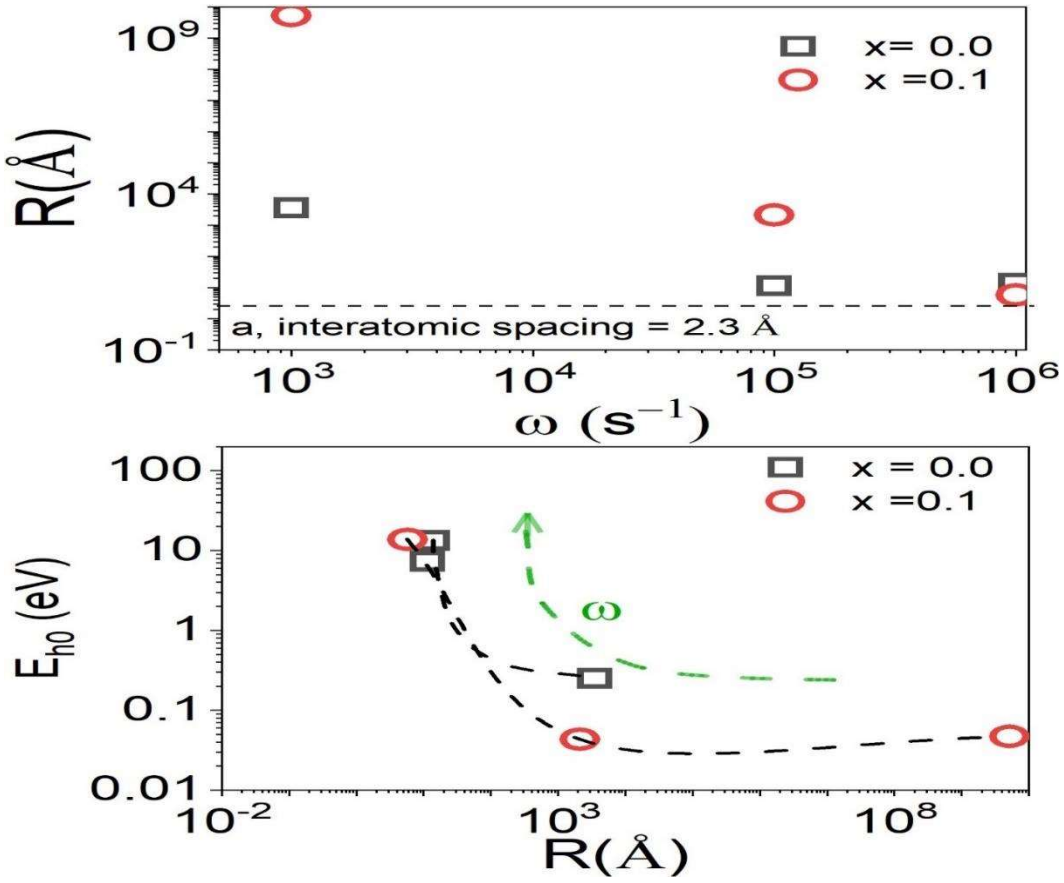


**Figure 5.11** a) Tunnelling distance with frequency and b) hopping energy with tunnelling distance at $\omega$ = $10^3$, $10^5$ and $10^6$($s^{-1}$).For x=0(square),x=0.1(circle) in $(La^{3+}_{1-x}Ca^{2+}_{x})_{9.67}(SiO_4)^{4-}_6O^{2-}_{2+\delta}$ system (lines are glide to eye)

~4.2 eV and 4.05 eV respectively suggesting the lowering of conduction band edge for x = 0.1. This is due to the interaction of Ca (s) and O(p) electrons (s-p interaction, fig 5.4 and its description). Further, to get the relative phonon contribution in these two samples, the data is fitted with free carrier absorption (FCA) equation $\alpha = \alpha_{AP}\,\lambda^{1.5} + \alpha_{OP}\,\lambda^{1.5} + \alpha_{IS}\lambda^{3.5} \approx \alpha_{AP}\lambda^{1.5} + \alpha_{OP}\lambda^{2.5} (if\ \alpha_{IS} \to 0)$ (Fig 5.12(c))[185] and found that scattering coefficient(SC) due to optical phonon scattering is reduced to ~1/2 while acoustic phonon scattering is reduced to nearly ~1/4 for x = 0.1. This explains the larger tunneling distance for x = 0.1 in acoustic frequency excitation (Fig. 5.11(a) and enhanced photo emission in optical absorption. The influence of phonon interaction and its different nature for the two samples can be observed in electric field dependent conductivity and therefore field dependent conductivity is plotted (Fig. 5.13). It is observed that for x =0, there is increase in conductivity for $E > 1.6kVm^{-1} > E_P$. While conductivity for x= 0.1 is slightly decreasing showing small mass enhancement in turn leading to slight reduction in mobility. But as the conductivity for x = 0.1 is still 100 times higher than x = 0 (see Fig. 5.13 inset), this suggests higher mobility confirming the formation of large polarons.

## 5.8 DISCUSSION

$(La^{3+}_{1-x}Ca^{2+}_{x})_{9.67}(SiO_4)^{4-}_{6}O^{2-}_{2+\delta}$ system shows push-pull and interstitial conduction mechanism governed with the formation of long pathways in O4 column. So far, in ionic solids, the evidences of structural disorder with ionic conductivity are least explored. In addition, like other ionic solids LSO is seen to have wide band gap of ~4.2eV and therefore ultra-wide band gap materials. In the ionic solids, the transport of large polarons at localized sites is coherent in adiabatic limits, which is similar to the motion of fermions in the delocalized states (but slower), therefore large polarons transport can be described in Drude-

like formalism (conductivity as a function of low frequency i.e., order of kHz). Our low frequency dependent conductivity study suggests that the conduction is occurring via overlapping large polaron tunnelling mechanism which can be explained through the classical model for bound and unbound continuum states of large polaron self-trapped carrier as explained earlier in Section C and here illustrated in Fig.5.14(a)

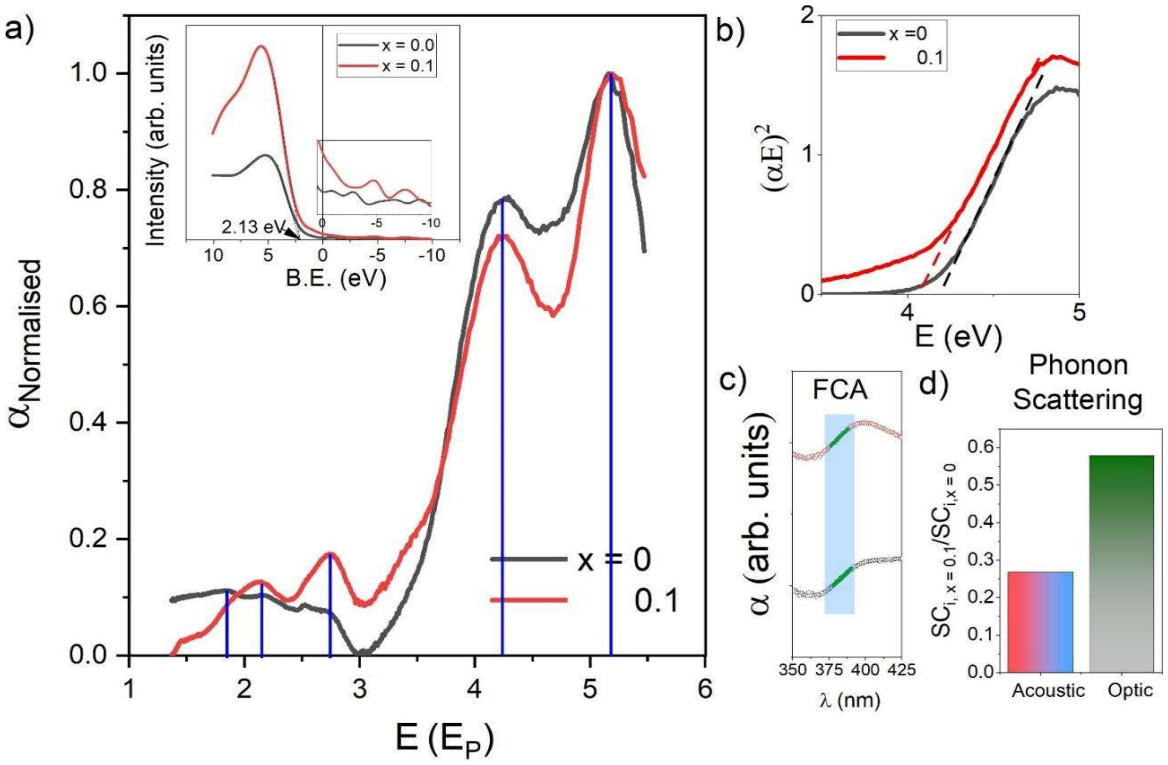


**Figure 5.12** (a) Variation of normalized optical (large polaron's) absorption for x=0.0 and x=0.1 in $(La^{3+}_{1-x}Ca^{2+}_{x})_{9.67}(SiO_4)^{4-}_{6}O^{2-}_{2+\delta}$ system(Inset) Valence band spectra using XPS study for both the samples along with zoomed valence band spectra in the negative binding region (b) Tauc plots for direct band gap is estimated 4.2 eV and 4.05 eV respectively suggested wider exciton energy for x = 0.1 (c) Free carrier absorption (FCA) fitting of the absorption obtained from UV-visible measurement for acoustic and optical phonon contributions (d) Ratio of phononic scattering coefficient (i = acoustic and optical phonon contributions) for x = 0.1 and x= 0.0.

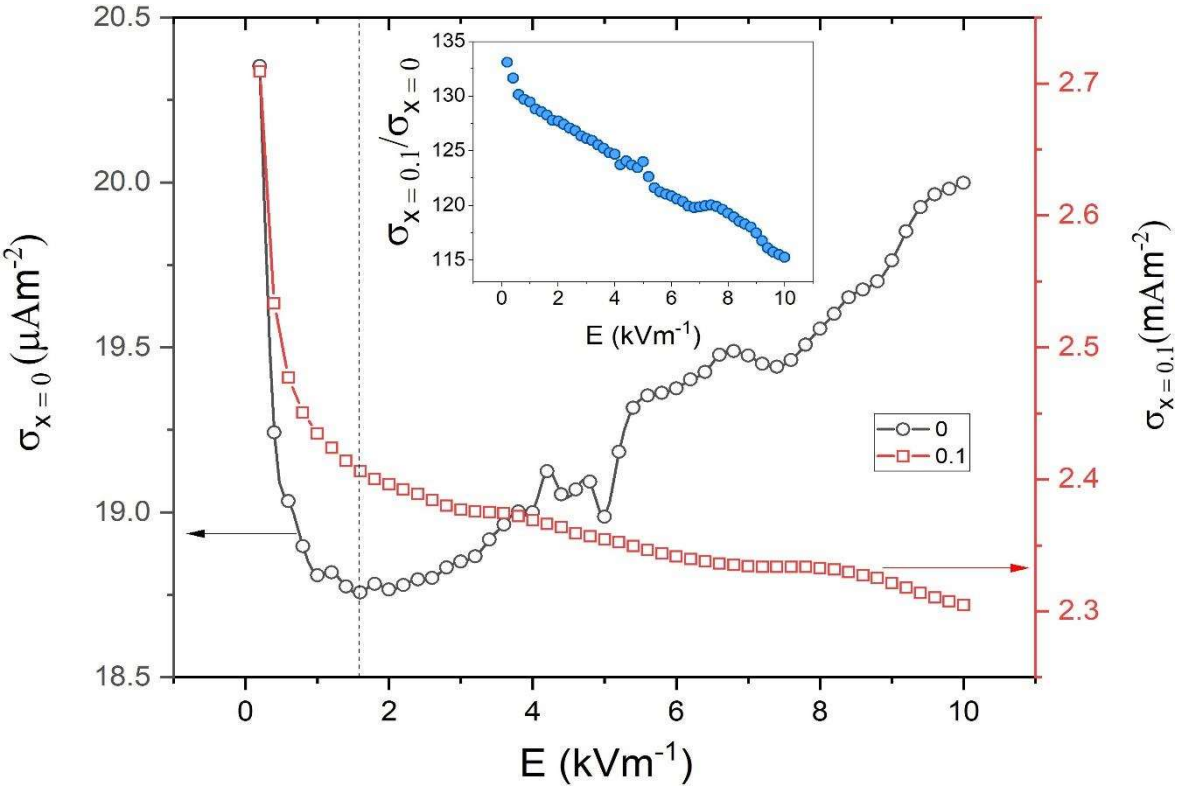


**Figure 5.13**. Field dependent conductivity for x=0.0 and 0.1 in $(La^{3+}_{1-x}Ca^{2+}_{x})_{9.67}(SiO_4)^{4-}_6O^{2-}_{2+\delta}$ system, inset shows the ratio of conductivity for x=0.1 and x=0.0

From the optical absorption and photoemission studies, we can estimate the electronic band structure. Fig.5.14(b) shows the difference between valence band and conduction band edge with fermi level and polaronic states and it can be seen that for x = 0.1, the conduction band is shifted towards the polaronic states rather than for x = 0.0. Moreover, the density of polaronic states is higher for x = 0.1 than x =0.0. Though Ca substitution at La site doesn't alter the structure significantly (negligible lattice alteration for x =0.1, which can be attributed to comparable ionic radii of $Ca^{2+}$ as compared to $La^{3+}$ (see supplementary Fig. 5.2)) but creates hole polarons. These hole polarons densify the polaronic states significantly. Fig.5.14 (c) shows unit cell structure in the x-y plane in this c -axis is into plane at corner occupied by O4 and surrounded by La1(6h) site as mentioned earlier and can be visualize in

central grey oval in 2 x 2 x 1 supercell (Fig 5.14(d)). Interestingly La2(4f) is almost collinear (~179.9°) along the c-axis. Our study suggests the probability of Ca-substitution on the La2 site is more. Thus without proper grain alignment in the c-axis[186] , mixed-channel conduction is achieved by suitable alteration of La2 site and hopping of oxygen is governed between the localized states generated due to La vacancies and oxygen content (long range diffusion in ab-plane by La vacancies and excess O ions). With the creation of La vacancies and hole polarons, hopping energy reduces. Further, scattering coefficient (SC) due to optical phonon scattering is reduced to 1/2 while acoustic phonon scattering is reduced to nearly 1/4 for x = 0.1. This explains the larger tunnelling distance and phonon amplitude enhancement for x = 0.1 inspite of having same activation and large polarons binding energy. Fig.5.14(d) illustrates the long channel formation in ab-plane and the vacancy diffusion of oxide ion in a-b plane apart from possible c-channel motion.

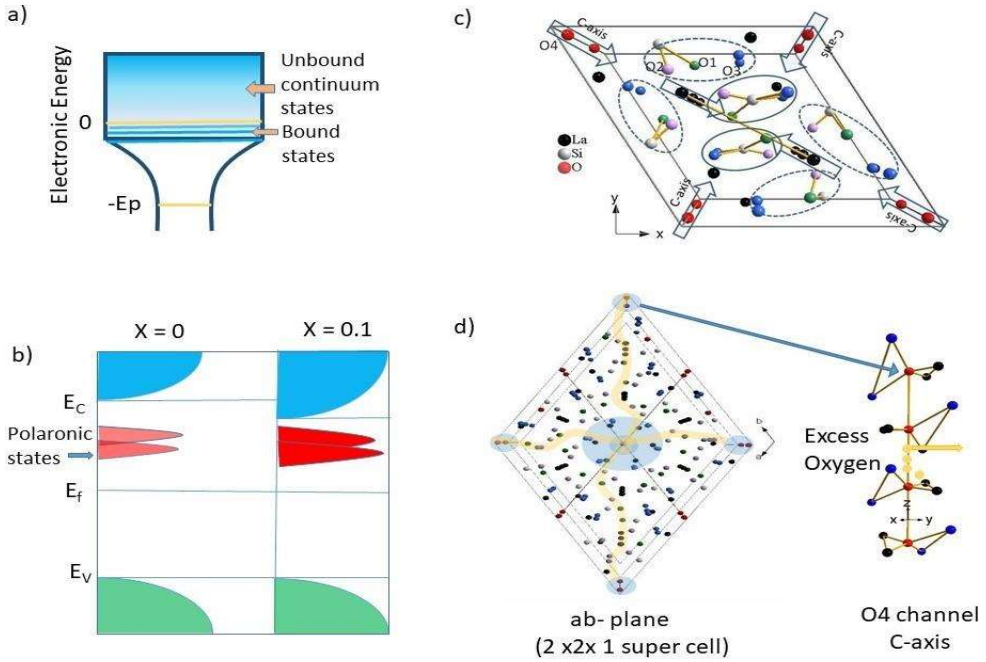

**Figure 5.14** (a) Classical model for bound and unbound continuum states of large polaron self-trapped carrier. (b) Illustration of difference in electronic band structure for x=0.0 and x=0.1 in $(La_{1-x}^{3+}Ca_x^{2+})_{9.67}(SiO_4)_6^{4-}O_{2+\delta}^{2-}$ system and polaronic states. (c) unit cell structure in the x-y plane in this c-axis is into plane at corner occupied by O4 and surrounded by La1(6h) site as mentioned earlier. (d) 2 x 2 x 1 supercell the long channel formation in ab-plane and increase in conductivity in apatite structure (O4-La1(6h) hexagon can be visualize in central gray oval)

## 5.9 CONCLUDING REMARKS

The lanthanum excess lanthanum silicate oxyapatite has shown higher oxide ion conductivity with lower activation energy and the activation energy increases with La vacancies (La at 4f site). We have obtained La deficient and O rich samples with Ca substitution (Ca has entered La vacancies and we believe that it has occupied La 4f site). Further, XPS and TGA con rm the formation of La deficient samples. The La(6h)-O4 bond length maximum at x = 0.1 suggests the formation of big La (6h) triangles that surround the O4 channel. The Si and O content is observed to increase and O vacancy is observed to decrease with the increase in x. Further, Na-KLL Auger peak of O diminishes with x. Simultaneously, intensity of satellite peak in Ca is increasing with x due to metal ligand interaction i.e. interaction of s- orbital of Ca and p-orbital of O (s-p interaction). The conductivity, due to connected grain growth increased for x = 0.1 which is higher than earlier report with Ca substitution can be attributed to the different local disorder by La and O occupancy. The conduction is occurring via overlapping large polaron tunnelling and the potential barrier is generated by the excess oxide ions that can show long range diffusion in the ab-plane through interstitials and La2 vacancy creation. This hopping of oxygen is governed between the localized states generated between La vacancies and oxygen content as

the interatomic spacing is higher than La1-O3 bond lengths for the samples. Further, the polaron radii reduce with Ca substitution and larger the polaron radius, higher will be the frequency exponent. This is showing the overlap of potential wells of the neighbouring sites (occupied and unoccupied sites) because of long range Coulomb interaction. Thus, with the creation of La -vacancies, hopping energy is reduced for x = 0.1. We found that for x = 0.0, scattering coefficient (SC) due to optical phonon scattering is reduced to 1/2 while acoustic phonon scattering is reduced to nearly 1/4 for x = 0.1. This study suggests that in apatite structure, ion conduction can be enhanced due to large polaron formation via phonon amplitude enhancement.